Dynamics of crustal compensation and its influences on crustal isostasy

Shijie Zhong

Seismological Laboratory, California Institute of Technology, Pasadena

Abstract. Deviation from isostasy is commonly believed to be caused by the strength of the Earth's lithosphere. An analysis of crustal compensation dynamics suggests that the deviation may have a dynamic origin. The analysis is based on analytic models that assume that (1) the medium is incompressible and has a layered and linear viscoelastic rheology and (2) the amplitude of topography is small compared with its wavelength. The models can describe topographic relaxation of different density interfaces at both small (e.g., postglacial rebound) and large time-scales. The models show that for a simple crust-mantle system with topography at the Earth's surface and Moho representing the only mass anomalies, while the crust always approaches the isostatic state at long wavelengths (>800 km), crustal isostasy may not be an asymptotic limit at short wavelengths, depending on crustal and lithospheric rheology. For a crust with viscosity smaller than lithospheric viscosity, at wavelengths comparable with widths of orogenic belts (i.e., <300 km), the crust tends to approach a state with significant overcompensation (i.e., excess topography at the Moho) within a timescale of about 10^7 years, and this characteristic time depends on wavelengths and crustal viscosity. This overcompensation is greater for weaker crust and stronger lithosphere. A thicker crust or lithosphere also enhances this overcompensation. If crustal and lithospheric viscosities are both large and comparable, the asymptotic state for the crust displays a slight undercompensation. For an elastic and rigid upper crust, the crust eventually becomes undercompensated after a characteristic decay time of topography at the Moho. The characteristic time is dependent on viscosity and thickness of the lower crust. The deviation from isostasy arises because these viscosity structures result in a ratio of vertical velocity at the surface to vertical velocity at the Moho which in the asymptotic state for short wavelengths differs from the ratio of density contrast at the Moho to that at the surface.

1. Introduction

Topography on the Earth's surface is directly related to crustal and mantle dynamics, which include crustal compensation, thermal subsidence [*Parsons and Sclater*, 1977], and viscous coupling of subcrustal mass anomalies [*Morgan*, 1965; *Hager and Richards*, 1989; *Gurnis*, 1993]. On continents, distinct topographic features including mountain belts are dominated by variations in crustal thickness through crustal compensation. Crustal compensation is effective in producing topography because of the proximity of crust-mantle boundary (i.e., Moho) to the Earth's surface and the large crust-mantle density difference. Complete crustal compensation (i.e., local Airy isostasy) is often assumed in continental dynamic models [*England and McKenzie*, 1982; *Wdowinski and O'Connell*, 1991; *Jones et al.*, 1996] and in retrieving continental dynamic topography (E.J. Vidale and W.D. Mooney, The Earth's topography: The influence of the crust and the mantle, submitted to *Nature*, 1996).

Isostasy is often defined as a condition or state of lithosphere under which no horizontal gradient in the lithostatic pressure exists below a certain depth (e.g., the depth of lithosphere) [e.g., *Daly*, 1940], although isostasy can be defined in other ways [*Dahlen*, 1982]. If only the mass anomalies associated with the two major density interfaces in the lithosphere (i.e., the Earth's surface and Moho) are considered, the isostasy would actually mean crustal isostasy which is possibly the most frequently used definition of isostasy. Admittedly, continental topography can also be partially compensated by other mass anomalies within lithosphere [e.g., *Banks et al.*, 1977; *Wernicke et al.*, 1996]. By measuring gravity and topography, one can check whether isostasy is satisfied as a condition for a given region. Although observations on North America [*Daly*, 1940; *Dorman and Lewis*, 1970; *Banks et al.*, 1977] and Australia [*Zuber et al.*, 1989] show that crustal isostasy explains long and intermediate wavelength Bouguer's anomalies, there are deviations from isostasy at short wavelengths (<400 km) in orogenic belts including Tibet [*Jin et al.*, 1994], eastern Tian Shan [*Burov et al.*, 1990], and the Appalachians [*McNutt*, 1980]. It has been long hypothesized that if lithosphere deviates from isostasy, the lithosphere will adjust itself to approach the isostatic state [*Daly*, 1940]. Postglacial rebound in Fennoscandia is an example of this isostatic adjustment [*Daly*, 1940].

Two mechanisms may cause crust to deviate from isostasy, even if only the mass anomalies at the Earth's surface and Moho are considered. First, the Earth's top layer may have a finite strength allowing it to permanently support deviatoric stresses at wavelengths comparable to elastic flexural wavelength of the top layer [*Barrell*, 1914; *Daly*, 1940; *Jeffreys*, 1970]. This mechanism can be conveniently modeled

with a thin elastic plate floating on an invisid medium [*Gunn*, 1943; *Heiskanen and Vening-Meinesz*, 1958; *Turcotte and Schubert*, 1982]. Second, *Artyushkov* [1974] indicated that because of the asymmetry in crustal compensation resulting from different density contrasts on the surface and Moho, a crust even in the state of isostasy may have a significant deviatoric stress (i.e., a nonequilibrium state), and the crust tends to be undercompensated at shortwavelengths. In essence, *Artyushkov*'s [1974] analyses questioned the validity of isostasy as a trend for lithosphere at short wavelengths.

The thin elastic plate model, combined with observed gravity and topography, has been extensively applied in many different regions to examine the isostasy and to infer lithospheric strength including stress and thickness. The inferred stress is often several kilobars in oceanic regions near seamounts and trenches [*Watts and Talwani*, 1974], which appears unrealistically large [*Kanamori*, 1980]. However, it has been found that the gravity and topography data can be explained equally well with other models employing plastic-elastic or viscous rheology but with significantly smaller stresses [*Liu and Kosloff*, 1978; *DeBremaecker*, 1977; *Melosh and Raefsky*, 1980; *Lambeck*, 1980]. More fundamentally, these plastic-elastic or viscous models imply that the lithosphere should deform dynamically under the high stress, contrary to the assumption of thin elastic models. Inferred elastic plate thicknesses range from zero to over 100 km for different regions [*Watts et al.*, 1980; *McNutt*, 1980; *Zuber et al.*, 1989; *Bechtel et al.*, 1991]. The inferred elastic plate thickness on the North American plate appears smaller for tectonically more active and higher heat flow regions (e.g., western United States) [*McNutt*, 1980; *Bechtel et al.*, 1991].

Laboratory studies on rock deformation have significantly advanced our understanding of mantle and crust rheology in the last two decades [*Byerlee*, 1978; *Brace and Kohlstedt*, 1980; *Carter and Tsenn*, 1987; *Karato and Wu*, 1993]. The upper crust, due to its lower temperature, may be dominated by brittle deformation. If stress is large, the upper crust displays significant vertical and horizontal deformation which are essential for mountain-building. If stress is smaller than a finite strength of crust (or faults), possibly in old and tectonically stable continental areas with small amplitude of topography, the stress may be supported by crust without producing any deformation. The lower crust and lithospheric mantle may behave as ductile flow under their temperature and pressure conditions. On continents, owing to the difference in temperature and composition between the lower crust and lithospheric mantle (i.e., quartz for the lower crust and olivine for mantle), the lower crust may be significantly weaker than lithospheric mantle, depending on heat flow [e.g., *Kusznir and Matthews*, 1988; *Bird*, 1991].

This multilayered structure with different deformation mechanism is significantly more complex than elastic plate models which implicitly assume a thin elastic layer overlying an invisid asthenosphere. Consequently, it is essential to understand how the multilayered structure of lithosphere and mantle influences crustal compensation and isostasy, so often considered with only thin elastic plate models. This is the main objective of this study. Previously, the influence of a weak lower crust on orogenic evolution has been considered in continental dynamic models [*Kusznir and Matthews*, 1988; *Bird*, 1991; *Avouac and Burov*, 1996]. By using semianalytic models that treat the upper crust as a thin elastic plate and the lower crust and mantle as a viscous medium, *Kusznir and*

Matthews [1988] showed that a weak lower crust could result in a flat Moho under orogenic belts, resembling the crustal structure under old mountain belts such as the Caledonides of Europe. Models that include crust and mantle with viscous rheology have also been used to study stress field in lithosphere [*Fleitout and Froidevaux*, 1982], topographic relaxation on Venus [*Grimm and Soloman*, 1988; *Bindschadler and Parmentier*, 1990], and tectonics of continental collision zones [*Lenardic and Kaula*, 1995].

In this paper, an analytic model coupling crust and mantle with a Maxwellian rheology is formulated to examine crustal compensation for different rheological structure. The equations of the mass and momentum conservation are solved to obtain the time evolution of topography at the top, Moho, and bottom boundaries, as well as the flow field, for any given initial topography at these density boundaries. The viscoelastic rheology naturally incorporates horizontal crustal deformation and elastic strength of highly viscous layers. The models indicate that at wavelengths comparable to width of orogenic belts (<300 km), the state of isostasy may be not the asymptotic limit for the crust and that the crust may approach a state with significant overcompensation or undercompensation on the Moho, depending on crustal and lithospheric rheology. The mechanism resulting in the non-isostatic state is different from that proposed by *Artyushkov* [1974]. The results for the cases with an effectively elastic upper crust are consistent with those from *Kusznir and Matthews* [1988]. In what follows, first, the basic formulation will be presented; second, results on crustal compensation for different models will be shown; finally, I will discuss the implications of the results to the Earth.

2. Physical Models and Analytic Approaches

2.1. General Description of Models

The models are in a two-dimensional Cartesian geometry bounded by two free surfaces (i.e., zero normal and shear stresses) at the top and bottom boundaries representing the Earth's surface and core-mantle boundary (CMB), respectively (Figure 1). The medium is assumed to be an incompressible viscoelastic fluid with a Maxwellian rheology and with arbitrarily layered elastic and viscosity structures. For simplicity, the models include two density layers (i.e., crust and mantle) and a constant shear modulus throughout the medium, but there can be any number of viscosity layers (Figure 1). The buoyancy forces include mass anomalies associated with topography at three density boundaries (i.e., the surface, Moho, and CMB), and for some cases mantle buoyancy (Figure 1). We seek the solution of time-dependent topography at the surface, Moho, and CMB as well as the flow field for given initial topography at these density boundaries and mantle buoyancy. It should be pointed out that for most cases with relatively small wavelengths (<1000 km) and shallow mass anomalies (<100 km in depth), topography at CMB is insignificant compared with topography at the surface and Moho and that CMB is included primarily for the completeness of formulation. The Earth's curvature is ignored in this study, but this should not influence the main results of this paper.

For most cases, the models include a crust with average thickness of 35 km, a lithospheric mantle with thickness of 65 km, and mantle extending from the bottom of lithosphere
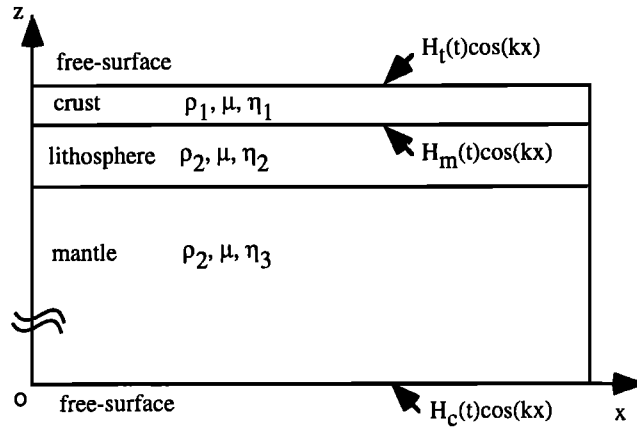
Figure 1. A viscoelastic model for topographic relaxation on the top surface, Moho, and core-mantle boundary.

to core-mantle boundary at 3000 km depth (Figure 1). Viscosity of the lithospheric mantle used in the models is about 10^{23} Pa s, and mantle viscosity is 10^{21} Pa s, both consistent with observations [*Walcott*, 1970; *Haskell*, 1936; *Cathles*, 1975]. Brittle deformation in the upper crust is approximated as viscoelastic deformation. Since this approximation may only be proper in a macroscopic sense, effective viscosity for the upper crust is difficult to constrain. A viscosity of 5×10^{23} Pa s is chosen for the upper crust to represent tectonically active regions with high stress and large deformation, and a viscosity of 5×10^{30} Pa s (i.e., effectively elastic) is used for the upper crust to represent tectonically stable regions with low stress. With a viscosity of 5×10^{23} Pa s, 100 MPa stress would result in approximately 10^{-16} s^{-1} strain rate, comparable with observed 10^{-15} s^{-1} to 10^{-16}s^{-1} strain rate on continents [*Eddington et al.*, 1987]. A wide variety of other rheological structure is also exploited.

2.2. Governing Equations and Solution Approach

Under the assumption of incompressibility, the momentum equation with no inertial forces and the continuity equation are

$$\nabla \cdot \hat{\sigma} - \rho g \vec{e}_z = 0, \qquad (1)$$

$$\nabla \cdot \vec{u} = 0, \qquad (2)$$

where ρ, g, and $\hat{\sigma}$ are the density, the acceleration of gravity, and the stress tensor, respectively; $\vec{u} = (u_x, u_z)$ is the flow velocity; $\vec{e}_z$ is the unit vector pointing upward (Figure 1); all the variables are a function of time t. The density and stress tensor for an incompressible Maxwell rheology may be expressed as

$$\rho = \rho_i + \delta\rho, \qquad (3)$$

$$\hat{\sigma} + \frac{\eta}{\mu}\dot{\hat{\sigma}} = -p\hat{I} + \eta\nabla\vec{u}, \qquad (4)$$

where ρ_i is the average density for the ith layer, $\delta\rho$ is the density anomaly, $\dot{\hat{\sigma}}$ is the time derivative of stress tensor, μ is the shear modulus, η is the dynamic viscosity, p is the pressure, and $\hat{I}$ is the identity matrix. After eliminating the hydrostatic pressure in the stress tensor, (1) becomes

$$\nabla \cdot \hat{\sigma} - \delta\rho g \vec{e}_z = 0. \qquad (5)$$

The general strategy for solving (2), (4), and (5) includes three steps. (1) The Laplace transform of these equations is taken to bring the variables from the time to the spectral domains. (2) The unknowns of the transformed equations are determined in the spectral domain. (3) A reverse Laplace transform is taken to bring the solutions back to the time domain. In order to linearize the boundary conditions facilitating analytic solutions, the assumption of a small ratio of topography to wavelength is used [e.g., *Cathles*, 1975]. The correspondence principle, normally used for solving viscoelastic problems [*Peltier*, 1974; *Wu and Peltier*, 1982], is not used here because for an incompressible medium (i.e., Possion's ratio is 0.5), solutions in the spectral domain can be easily derived (the Appendix). However, for a compressible viscoelastic medium, the correspondence principle is needed [*Peltier*, 1974]. In the approach used here, kinematic conditions are used to relate topography to flow velocity on each density boundary, so that topography is solved directly (the Appendix). A Fourier's series is used to represent the solutions for each wavelength in the spatial domain (the Appendix). For a surface relaxation problem in an isoviscous medium with a uniform density, our solution is identical to the half-space solution of *Wu* [1992] for relatively short wavelengths.

3. Results and Discussion

In this section, a simple two-layer model is first used to demonstrate the basic physics of crustal compensation. The influence of lithospheric and crustal rheology on crustal compensation will be considered in models with relatively weak and strong upper crust. Effect of mantle buoyancy will be investigated before discussing the overall implications of the work.

3.1. Two-Layer Model and Comparison With Thin Elastic Plate

For this two-layer model (model 1), viscosities for crust and mantle are 5×10^{23} Pa s and 10^{21} Pa s, respectively, and crustal thickness is 35 km (Tables 1a and 1b). Initial topography is zero at the Moho but 3 km at the top surface (i.e., H_t^0 in equation (A9) is 3 km). For a wavelength of 400 km, both the Moho and top surface initially experience a uniform subsidence, and at about 3×10^6 years after the loading, the Moho and top surface approach a state with a degree of compensation, D, of 0.997, indicating nearly complete isostasy (Figure 2a). Degree of compensation, D, is defined as the ratio of excess mass at the Moho to that at the top surface [*Turcotte and Schubert*, 1982]. After 3×10^6 years, D remains constant, while the Moho and surface topography diminish

Table 1a. Physical and Parameters

Parameter	Value
Crust density	2.8e3 kg m^{-3}
Mantle density	3.3e3 kg m^{-3}
Outer core density	6.6e3 kg m^{-3}
Acceleration of gravity	10 m s^{-2}
Shear modulus	1.5e11 Pa
Possion's ratio	0.5

Read 2.8e3 as 2.8 x 10^3.

Table 1b. Geometrical Model Parameters

Model	Layer 1	Layer 2	Layer 3	Layer 4	Layer 5	MB
1	5e23 (0-35)	1e21 (35-3000)	--	--	--	no
2	5e23 (0-20)	1e21 (20-35)	5e23 (35-55)	1e23 (55-100)	1e21 (100-3000)	no
3	5e23 (0-20)	1e21 (20-50)	5e23 (50-70)	1e23 (70-115)	1e21 (115-3000)	no
4	5e30 (0-20)	1e21 (20-35)	5e23 (35-55)	1e23 (55-200)	1e21 (200-3000)	no
5	5e23 (0-20)	1e21 (20-35)	5e23 (35-55)	1e23 (55-100)	1e21 (100-3000)	yes

MB stands for mantle buoyancy. Viscosity (in pascal seconds) and depth range (in parentheses with unit of kilometers) for each layer are given. Read 5e23 as 5×10^{23}.
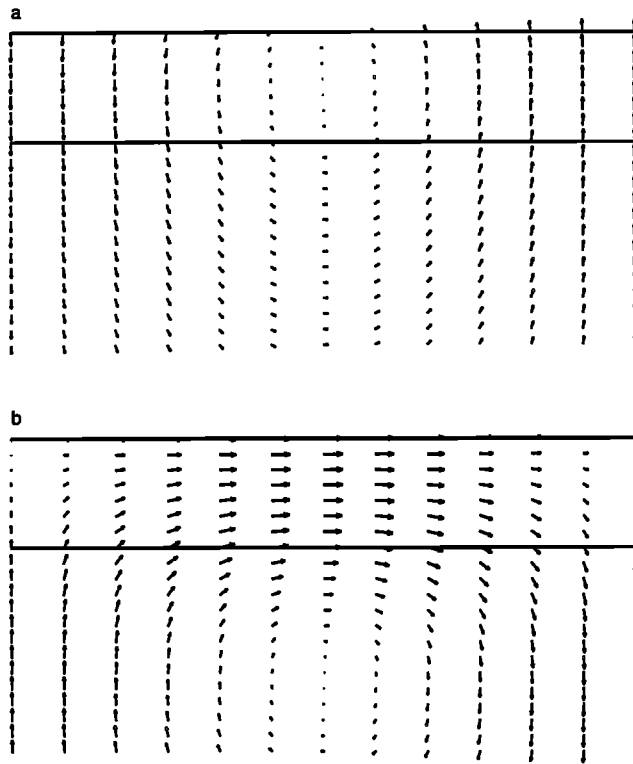
with time (Figure 2a). Flow fields for the top 100 km layer at two different instants in time (Figure 2a for time marks) show that flow within the crust is dominated by vertical motion at the early stage (Figure 3a) and by horizontal motion after D becomes constant (Figure 3b). The horizontal crustal deformation reduces the crustal thickness variation (Figure 3b).

For this two-layer model with three density boundaries, there are five different deformation modes (the Appendix). From Figure 2a, two distinct deformation modes can be identified. The first mode with the longest characteristic time τ_1 (4.3×10^8 years) is associated with horizontal crustal deformation that reduces the crustal thickness variation (e.g., Figure 3b). The second mode with the second longest characteristic time τ_2 (5.3×10^5 years) is related to vertical deformation which leads the Moho and surface to the state with constant D. The other three modes with much shorter characteristic times also contribute to the vertical deformation (e.g., Figure 3a). τ_2 increases with decreasing wavelength, but it is always significantly smaller than τ_1 which is insensitive to wavelength (Figure 2b). Both τ_1 and τ_2 increase with crustal viscosity, but the other three short characteristic times are dependent on mantle viscosity and are insensitive to crustal viscosity. Deformation associated with the modes other than τ_1 has been extensively discussed in glacial rebound studies [*Cathles*, 1975; *Wu and Peltier*, 1982]. The horizontal crustal flow is discussed in previous studies [*Artyushkov*, 1974]. D in an asymptotic state is close to unity for wavelengths from 6000 km to 200 km for model 1 (Figure 2b), indicating that crustal isostasy is the asymptotic state at these wavelengths. At shorter wavelengths, it takes a longer time for the crust to reach the constant D state (Figure 2b).

The results from the viscoelastic models may be compared with thin elastic plate models. Thin elastic plate models do not account for creep deformation and vertical variation in stress [e.g., *Turcotte and Schubert*, 1982]. For a thin elastic plate model, if the elastic plate is assumed to have the same elastic properties as in model 1 (table 1a) with a thickness of 35 km, degree of compensation is significantly smaller than 1.0 for wavelengths less than 1000 km (Figure 2c).
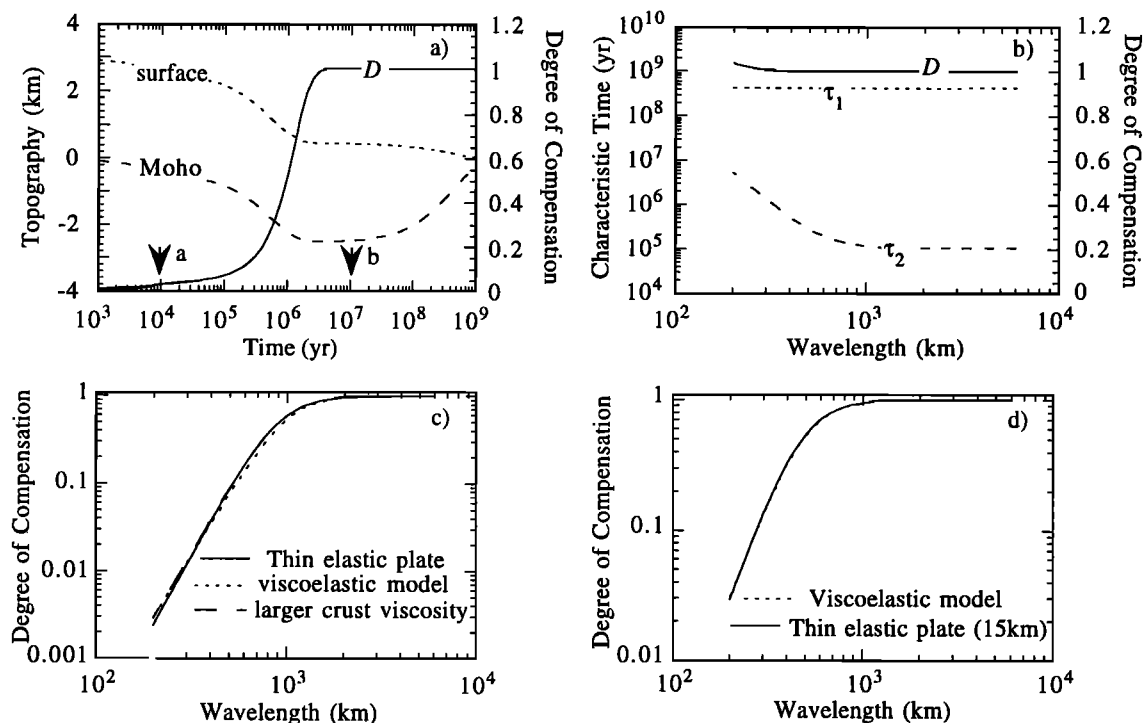
Figure 2. (a) Time history of Moho and surface topography and degree of compensation D for model 1 with 400 km wavelength; (b) wavelength dependence of two longest characteristic times τ_1 and τ_2 and D at an asymptotic state for model 1; and comparisons of D between viscoelastic models and thin elastic plate models for (c) 35 km thick crust and (d) 15 km thick crust.

Figure 3. Flow fields at (a) 10^4 years and (b) 10^7 years for model 1 with 400 km wavelength (time marks in Figure 2a). The maximum velocities are 1.975 cm/yr and 0.00128 cm/yr in Figures 3a and 3b, respectively. Only the flow fields in the top 100 km for the half wavelength are shown. The solid lines represent the locations of the surface and Moho.

Comparison can be made between the viscoelastic and thin elastic plate models if a very large viscosity contrast between crust and mantle is used in viscoelastic models. That is to assume τ_1 and τ_2 in Figure 2b to be infinite; accordingly, degree of compensation can be computed from the eigenfunctions of these two modes (see (A20) in the Appendix).
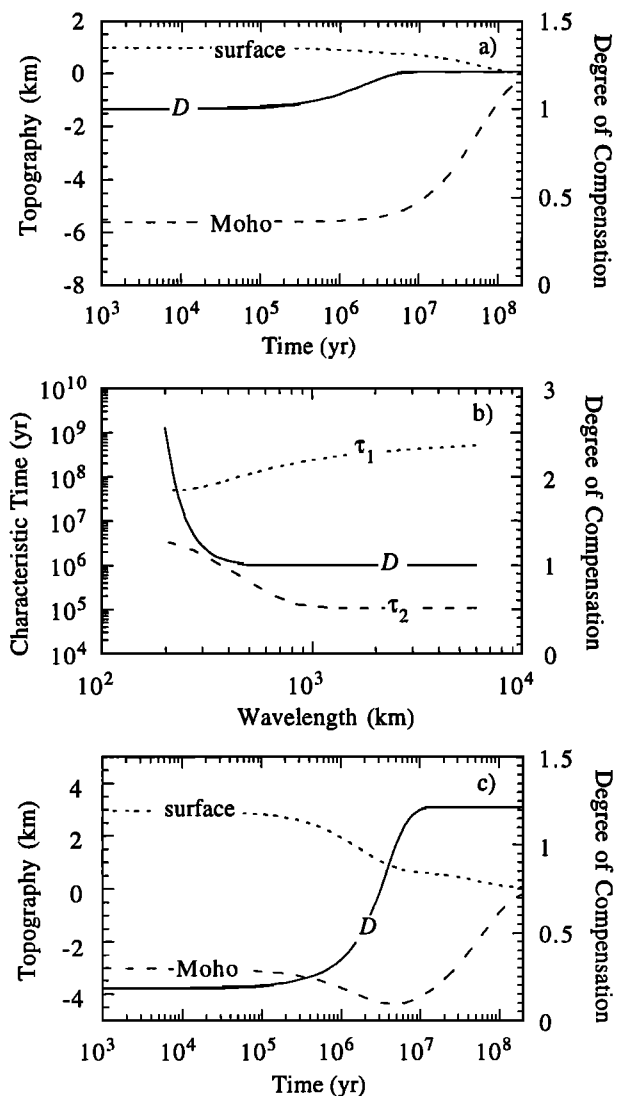
For model 1, degree of compensation differs from the thin elastic plate model at both intermediate and short wavelengths (Figure 2c). To increase crustal viscosity to 5×10^{24} Pa s reduces the difference at intermediate-wavelengths but increases the difference at short wavelengths (Figure 2c). The difference in D is more than 20% for wavelengths shorter than 230 km (Figure 2c) and cannot be reduced by further increasing viscosity contrast between crust and mantle. However, for reduced crustal thickness and elastic plate thickness (15 km), viscoelastic (5×10^{24} Pa s for crust and 10^{21} Pa s for mantle) and thin elastic plate models agree with each other for wavelengths from 6000 km to 200 km (Figure 2d). This suggests that the difference in D at short wavelengths in Figure 2c is caused by ignoring vertically varied stress in thin plate approximation.

3.2. Models With Moderately High Viscosity Upper Crust

Studies on crustal rheology indicate that the lower crust may be weaker than mantle and upper crust [*Brace and Kohlstedt*, 1980]. In model 2, the viscosities for the upper and lower crust

are assumed to be 5×10^{23} Pa s and 10^{21} Pa s, respectively, and the viscosity for mantle lithosphere varies from 5×10^{23} Pa s to 10^{23} Pa s (Table 1b). The thickness for the upper and lower crust are 20 km and 15 km, respectively (Table 1b). The initial Moho and surface topography are assumed to be isostatic with 1 km topography at the surface. For 300 km wavelength, Moho and surface topography monotonously decrease with time, and Moho topography is reduced to one third of its initial value after 6×10^7 years (Figure 4a). However, D drifts from the initial 1.0 to 1.21 after 4×10^6 years and D remains as 1.21, independent of amplitude of topography (Figure 4a). This indicates that for the given rheological structure and wavelength, the state of isostasy is intrinsically not an asymptotic limit, and the crust tends to be overcompensated at the asymptotic state.

Deviation from isostasy at the asymptotic state is greater for shorter wavelengths, but isostasy remains valid within 5%
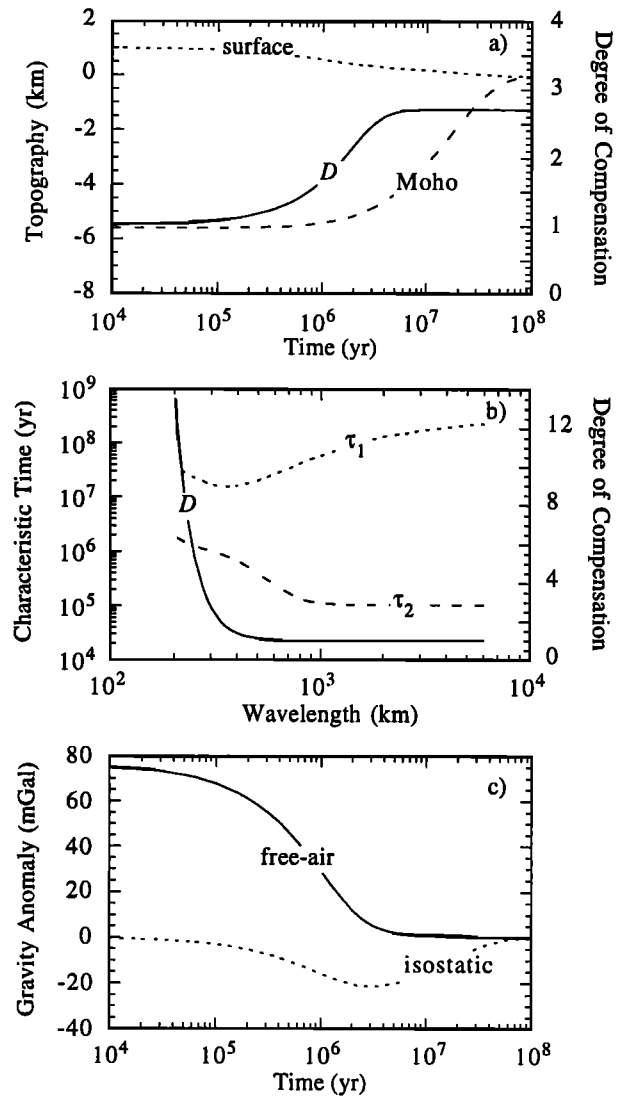

Figure 4. (a) Time history of Moho and surface topography and degree of compensation D for model 2 with 300 km wavelength and initially isostatic crust; (b) wavelength dependence of two longest characteristic times τ_1 and τ_2 and D at an asymptotic state for model 2; and (c) time history of Moho and surface topography and degree of compensation D for model 2 with 300 km wavelength and initially non-isostatic crust.

for wavelengths longer than 400 km (Figure 4b). The time τ_1 decreases with decreasing wavelength and reverses this trend at a wavelength of 240 km (Figure 4b), displaying properties of a channel flow [*Cathles*, 1975]. τ_2 increases with decreasing wavelength (Figure 4b), similar to model 1 (Figure 2b). It should be emphasized that D at the asymptotic state does not depend on initial conditions which only influence D in the first several million years, depending on wavelength, as demonstrated by a case which only differs from the calculation in Figure 4a by having initial 3 km and -3 km topography at the top and Moho, respectively (Figure 4c).

To understand the controls on deviation from isostasy, cases with different rheological structure are computed. In each of these cases, only one model parameter is allowed to differ
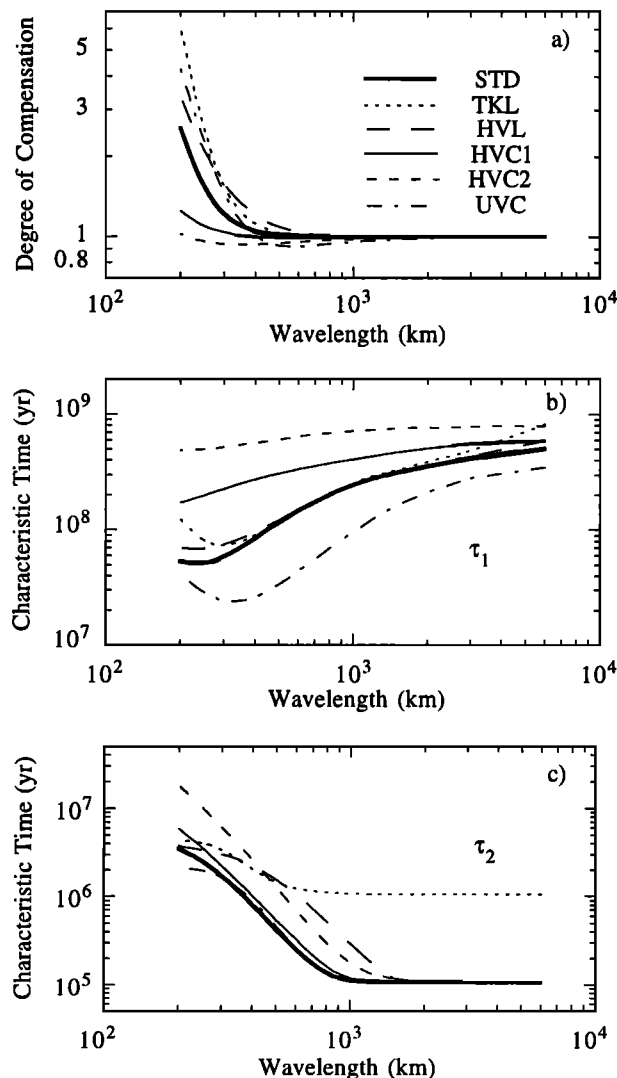
Figure 5. Wavelength dependence of (a) D at an asymptotic state, (b) τ_1, and (c) τ_2 for six different cases. STD is for model 2. For TKL, HVL, HVC1, and HVC2, each of these four cases differs from model 2 in only one model parameter. TKL is for the case with 200 km thick lithosphere; HVL is for the case with 5×10^{24} Pa s viscosity for the upper lithosphere; HVC1 and HVC2 are for the cases with 10^{22} Pa s and 5×10^{23} Pa s viscosity for the lower crust, respectively. UVC case is identical to model 2 except that the upper and lower crust have the same viscosity 10^{22} Pa s.

Figure 6. (a) Time history of Moho and surface topography and degree of compensation D for model 3 with 300 km wavelength and initially isostatic crust; (b) wavelength dependence of two longest characteristic times τ_1 and τ_2 and D at an asymptotic state for model 3; and (c) time history of free-air and isostatic anomalies for the same calculation in Figure 6a.

from model 2. If lithospheric viscosity is increased, the wavelength at which isostasy cannot be attained increases, and the deviation from isostasy increases (Figure 5a). A thicker continental lithosphere (200 km) has a similar effect than a larger lithospheric viscosity (Figure 5a). However, as the lower crust viscosity increases, deviation from isostasy decreases (Figure 5a). When the lower and upper crust have the same viscosity (5×10^{23} Pa s), D shows a nearly complete isostasy for all the wavelengths only with a slight undercompensation for wavelengths from 200 km to 800 km (Figure 5a). The degree of undercompensation does not increase with further increase in crust viscosity. For these cases, τ_1 and τ_2 are generally longer than those in model 2 (Figures 5b and 5c). Particularly, a thicker continental lithosphere increases τ_2 substantially at long wavelengths, and a larger lower crust viscosity increases τ_2 at short wavelengths (Figure 5c).

A significant overcompensation at short wavelengths is also observed for a case which includes a crust with uniform strength (10^{22} Pa s for both the upper and lower crust) but is otherwise identical to model 2 (Figure 5a), suggesting that the overcompensation occurs as long as the overall strength of crust is weaker than lithospheric mantle. The reduced viscosity for the upper crust yields a smaller τ_1 (Figure 5b), indicating that crustal thickness variation decays more rapidly. The influence of mantle viscosity is studied with a case that includes a weak asthenosphere and a high viscosity lower mantle (i.e., 10^{20} Pa s between 100 km and 400 km, 10^{21} Pa s between 400 km and 670 km, and 10^{22} Pa s below 670 km) but is otherwise identical to model 2. Mantle viscosity structure only influences deformation modes with short characteristic times and does not have noticeable effects on eigenfunctions associated with τ_1 and τ_2 and hence D.

The influence of a thicker lower crust is considered in model 3. In model 3, the thickness of the lower crust is increased to 30 km, while thicknesses of the other layers in lithosphere remain the same as those in model 2 (Table 1b); viscosities for each layer are the same as in model 2 (Table 1b). For model 3 with 300 km wavelength and initially isostatic crust, a state with constant D is reached after 4×10^6 years with a greater deviation from isostasy than Model 2 (Figures 4a, 4b, 6a and 6b). For model 3, τ_1 and τ_2 are both reduced (Figure 6b). The reduced characteristic times suggest that any crustal thickness variation at a few hundred kilometers wavelength would vanish within about 2×10^7 years. The implications of the rapid decay in crustal thickness variation to continental topography were discussed by *Bird* [1991] and *Avouac and Burov* [1996]. For 300 km wavelength, after 2×10^6 years, the free-air gravity

anomaly decreases to about 10 mGal, but the magnitude of isostatic anomaly (negative) increases to 20 mGal (i.e., the peak-to-peak magnitude is 40 mGal) and the significant isostatic anomaly can last for more than 10^7 years (Figure 6c).

3.3. Models With Effectively Elastic Upper Crust

Tectonically stable continental regions with a small stress may have a strong upper crust and thick lithosphere. In model 4, the effective viscosity for the upper crust is assumed to be 5×10^{30} Pa s (i.e., effectively elastic for the time period considered here), and the thickness of continental lithosphere is 200 km (Table 1b). Other model parameters are the same as those in model 2. Since models with deformable upper crust (i.e., 5×10^{23} Pa s) in section 3.2 mainly suggest two states for crustal compensation: overcompensation and isostasy (Figure 5a), we will use these two states as initial conditions for calculations in this section.

For 300 km wavelength and an initially isostatic crust with 1 km surface topography, the crust becomes moderately overcompensated between 10^6 and 10^7 years and then becomes significantly undercompensated after 10^8 years (Figure 7a). While the Moho topography diminishes at about 3×10^8 years, surface topography is about 0.72 km that can be permanently supported by strength of the upper crust (Figure 7a). The two modes with longest characteristic times τ_1 and τ_2 for 300 km wavelength are 10^6 and 8.6×10^7 years (Figure 7b). The duration of the over-compensation period is controlled by τ_1 and τ_2. Similar to that in section 3.2, deformation associated with τ_1 mode reduces crustal thickness variation (Figures 4a and 7a). However, for model 4 with an effectively elastic upper crust, only Moho topography approaches to zero, and surface
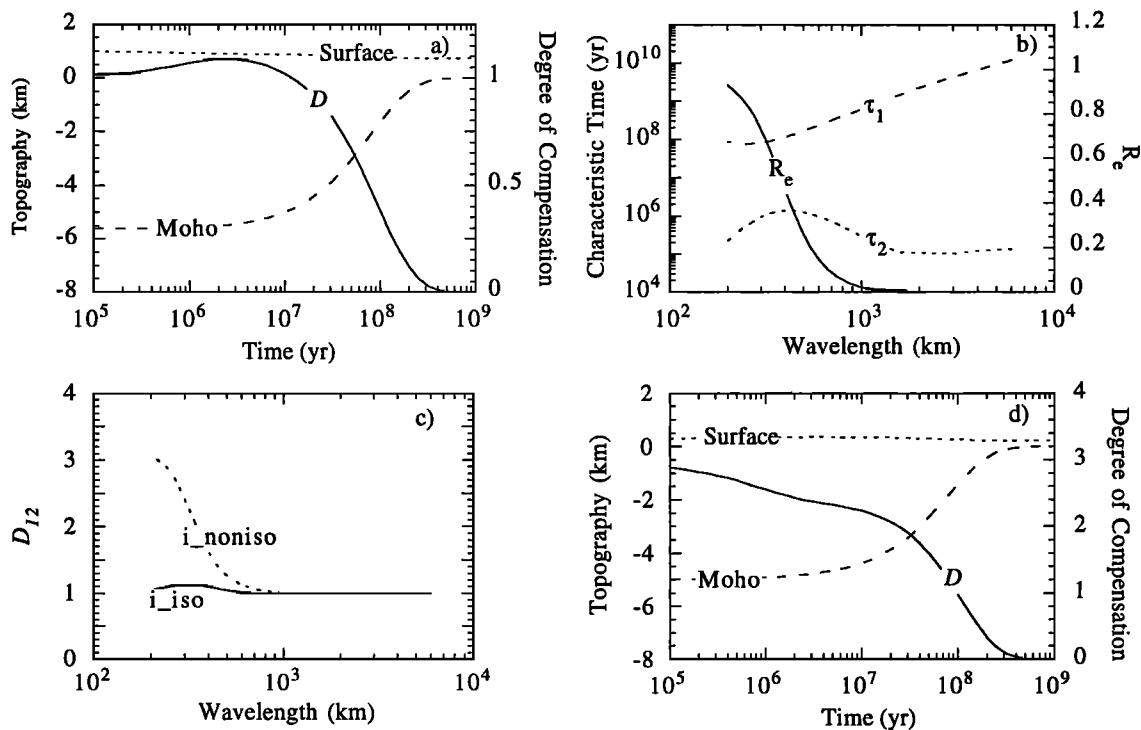

Figure 7. (a) Time history of Moho and surface topography and degree of compensation D for model 4 with 300 km wavelength and initially isostatic crust; (b) wavelength dependence of two longest characteristic times τ_1 and τ_2 and R_e for model 4; (c) wavelength dependence of D_{12} between τ_1 and τ_2 for model 4 with initially isostatic (i_iso) and non-isostatic crust (i_noniso); and (d) time history of Moho and surface topography and degree of compensation D for model 4 with 300 km wavelength and initially non-isostatic crust.

topography will be reduced to a value that can be elastically supported by the upper crust.

The time τ_1 is strongly dependent on wavelength and varies from 10^{10} years for 6000 km wavelength to 9×10^7 years for 200 km wavelength (Figure 7b); τ_2 is about 10^5 years for long wavelength; and τ_2 increases to about 1.3×10^6 years at 400 km wavelength and then decreases with decreasing wavelength (Figure 7b). Degree of compensation between τ_1 and τ_2, D_{12}, is close to 1.0 for all wavelengths, similar to its initial value (i.e., the solid line in Figure 7c). After τ_1, crust becomes undercompensated for all wavelengths, but the elastically supported surface topography is insignificant for wavelengths longer than 1000 km, as indicated by the ratio of elastically supported topography to initial topography at the surface, R_e (Figure 7b). The elastically supported topography increases for decreasing wavelength (Figure 7b), consistent with thin elastic plate models [e.g., *Turcotte and Schubert*, 1982].

If the initial topography at the surface and Moho for 300 km wavelength are 0.3 km and 5 km (i.e., initially overcompensated with $D=2.976$), respectively, the crust remains over-compensated between 10^6 and 2×10^7 years with $D \sim 2.3$ (Figure 7d). However, crust becomes greatly undercompensated at 2×10^8 years (Figure 7d), similar to the calculation with an initially isostatic crust (Figure 7a). Surface topography increases to about 0.36 km at 4×10^6 years, and then starts to decrease (Figure 7d). After 3×10^8 years, the surface topography is reduced to 0.22 km that is permanently supported by the elastic strength of the upper crust (Figure 7d). For wavelengths longer than 1000 km, D_{12} between τ_1 and τ_2 is close to 1.0; for wavelengths less than 400 km, D_{12} is larger than 1.5 (i.e., dashed line in Figure 7c). For long wavelengths, isostasy can be restored shortly ($\sim 10^5$ years) after the initial non-isostatic state, and the isostasy can be maintained for 10^9 years before crustal thickness variation diminishes (Figure 7c for D_{12}, and Figure 7b for τ_1, τ_2, and R_e which do not vary with initial conditions). D_{12} for short wavelengths depends on initial conditions (Figure 7c), indicating that the influence of initial conditions at short wavelengths can last for a long time, but crust always becomes undercompensated after τ_1.

Influences of viscosity in the lower crust, thickness of the upper and lower crust, and lithospheric thickness are investigated with four more calculations for the initially overcompensated crust ($D=2.976$). In each calculation, only one model parameter differs from model 4. Compared with model 4 (STD in Figure 8), a thicker crust (TKC1 and TKC2 in Figure 8a) increases D_{12} between τ_1 and τ_2 at short wavelengths; a more viscous lower crust (HVC in Figure 8a) reduces D_{12} at short wavelengths. Compared with model 4, τ_1 for a thicker lower crust is reduced significantly for wavelengths larger than 300 km (TKC1 in Figure 8b); τ_1 for the more viscous lower crust is increased at all wavelengths (HVC in Figure 8b). However, neither a thicker upper crust (TKC2 in Figure 8b) nor a thinner continental lithosphere (TNL in Figure 8b) influences τ_1 significantly (Figure 8b); τ_2 is always less than 2.4×10^6 years (Figure 8c). These results indicate that crust with an elastic upper crust and viscous lower crust can keep its initial state (i.e., isostatic or overcompensated) at short wavelengths for a long period in time before the crust eventually becomes significantly undercompensated. The more viscous the lower crust, the longer the crust can maintain its initial state, but a thicker lower crust has an opposite effect.
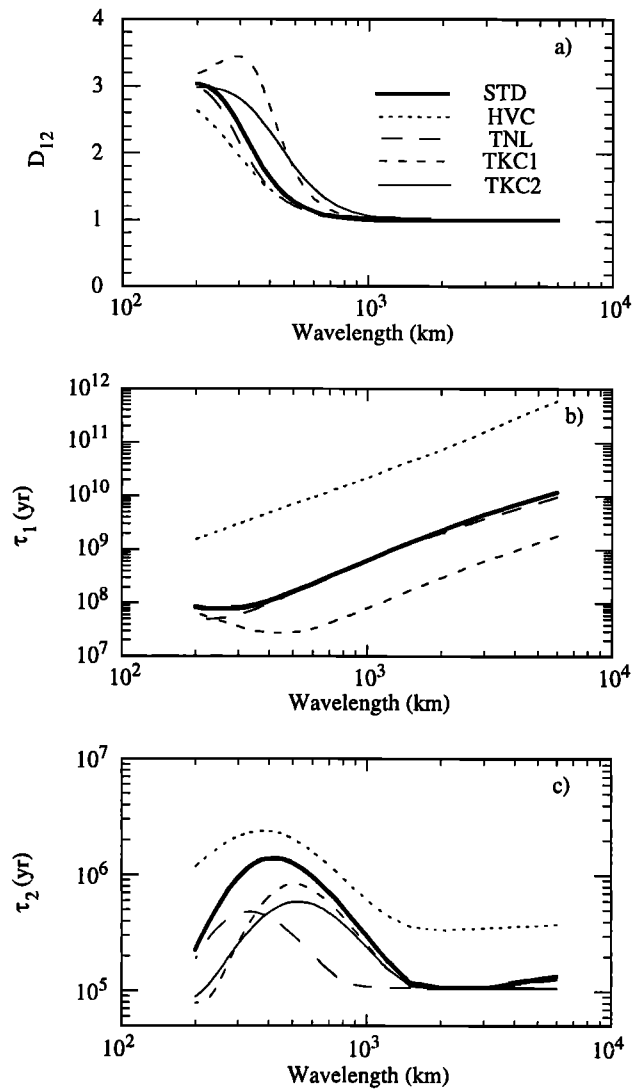

Figure 8. Wavelength dependence of (a) D_{12} for initially non-isostatic crust, (b) τ_1, and (b) τ_2 for five different cases. STD is for model 4. Each of the other four cases differs from model 4 in only one model parameter. HVC is for the case with 5×10^{23} Pa s viscosity for the lower crust; TNL is for the case with 100 km thick lithosphere; TKC1 is for the case with a 30 km thick lower crust; and TKC2 is for the case with a 35 km thick upper crust.

3.4. Influences of Mantle Buoyancy on Crustal Compensation

In this section, two specific questions will be addressed: (1) influence of mantle buoyancy forces on crustal compensation and (2) retrieval of dynamic topography and geoid derived from mantle buoyancy. Model 5 includes the same rheological structure as in model 2 but with additional mantle buoyancy (Table 1b). Two different wavelengths 300 km and 3000 km will be considered. For 300 km wavelength, the mantle buoyancy is assumed to locate at a depth of 200 km with a surface density of 8.25×10^4 kg m^{-2}, and for 3000 km wavelength, the mantle buoyancy is at a depth of 500 km with a surface density of 1.65×10^4 kg m^{-2}. The shallower and larger mantle buoyancy for 300 km wavelength is used to produce a comparable dynamic topography with that for 3000 km wavelength.
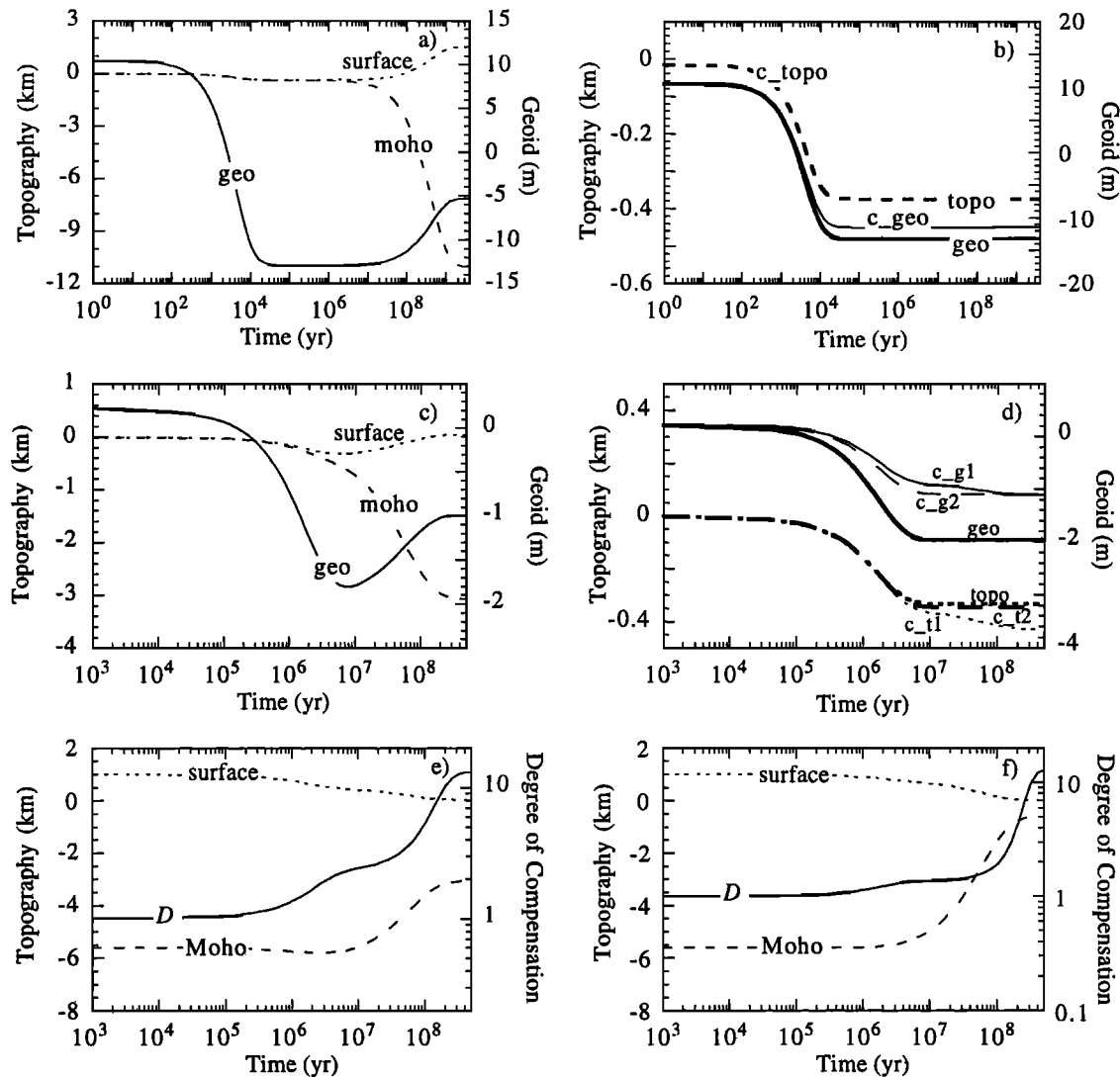
Fig. 9. (a) Time history of Moho and surface topography and geoid for model 5 with mantle buoyancy for 3000 km wavelength and (b) the corresponding corrected topography and geoid; (c) time history of Moho and surface topography and geoid for 300 km wavelength and (d) the corresponding corrected topography and geoid. Also shown in Figures 9b and 9d are time history of topography and geoid (thick lines) for calculations that exclude the crust but otherwise are identical to the calculations in Figures 9a and 9c. Time history of Moho and surface topography and D for model 5 that includes (e) initially isostatic crust and mantle buoyancy for 300 km wavelength, and (f) with reduced mantle buoyancy. In Figures 9b and 9d, c_t and c_g stand for corrected topography and geoid with $D=1$. In Figure 9d, c_t1 and c_g1 are for corrected topography and geoid with $D=1.21$.

For 3000 km wavelength with zero initial topography at the Moho and surface, the Moho and surface subside at a similar rate before Moho and surface topography reach about -0.37 km at 2×10^4 years (Figure 9a). After about 10^6 years, while the Moho continues to subside, the top surface starts to rebound (Figure 9a). At about 10^9 years, Moho and surface topography stabilize at -11 km and 1.5 km, respectively (Figure 9a). This result indicates that a topographic high can be generated over a negatively buoyant mass anomaly if the mantle flow generated by the mass anomaly shears the crust for a sufficiently long period of time. A similar result was reported by Bindschadler and Parmentier [1990] in a half-space viscous model for topographic evolution on Venus. By examining the Moho and surface topography (Figure 9a), crustal isostasy as a condition is clearly violated. The geoid over the negatively buoyant mass anomalies is initially 10 m,

but the geoid becomes -13 m after the top and Moho surfaces are depressed to -0.37 km at 2×10^4 years (Figure 9a). The geoid starts to decrease after 10^6 years and it stabilizes at about -5 m after 10^9 years (Figure 9a). The variation in geoid reflects the topographic variations at the surface, Moho, and core-mantle boundary.

For a long wavelength, since crustal isostasy is expected if no external force acts on crust (e.g., Figure 5a), one may perform isostatic corrections on topography and geoid to retrieve the topography and geoid derived solely from subcrustal buoyancy. In retrieving corrected topography, our approach is similar to that of Vidale and Mooney [1996] and consists of three steps: (1) compute the compensated topography on the top surface based on the Moho topography, assuming ideal crustal isostasy; (2) subtract the compensated topography determined from step 1 from surface

topography; and (3) convert the resulting topography onto a surface that has a density contrast ρ_m. The corrected topography is $H_{corr} = [H_t + (\rho_m/\rho_c - 1)H_m]\rho_c/\rho_m$. The corrected geoid is obtained with two steps, similar to those of *Chase and McNutt* [1982]: (1) compute the corresponding Moho topography based on surface topography, assuming ideal crustal isostasy; and (2) correct out the geoid associated with the surface topography and the Moho topography computed in step 1. In above procedures, while crustal structure is needed for computing the corrected topography, the only information required for the corrected geoid is the surface topography.

The corrected topography and geoid for 3000 km wavelength do not show any variations after 2×10^4 years (Figure 9b). Compared with a case that only differs from the current calculation in excluding the crust, the corrected topography is nearly identical, but the corrected geoid is about 15% smaller after 2×10^4 years (Figure 9b). For 300 km wavelength with the same initial conditions, surface and Moho topography and geoid evolve in a similar way to those for 3000 km wavelength (Figure 9c). However, corrected topography and geoid differ significantly from those for a calculation without crust (Figure 9d). This may be because crustal isostasy does not hold as a trend at this short wavelength (Figure 4a). Interestingly, if the corrections are made with $D=1.21$ which is the trend of crustal compensation at 300 km wavelength with the same rheological structure (Figure 4a), the corrected topography agrees well with that for the calculation without crust, but corrected geoid is about 50% smaller (Figure 9d).

The influences of mantle buoyancy on crustal compensation depend on relative strength between mantle buoyancy and crustal buoyancy. Compared with the calculation in Figure 4a, if an additional mantle buoyancy with a surface density of 8.25×10^4 kg m^{-2} is included at 200 km depth, Moho and surface topography and D show quite different time history (Figure 9e). A state with constant D is achieved after 2×10^8 years with D greater than 10 (Figure 9e). The Moho and surface topography at this constant D state are only dependent on the mantle buoyancy. The time it takes to reach this state is determined by τ_1 (Figure 4b for 300 km wavelength). D is about 2 between 4×10^6 and 3×10^7 years (Figure 9e), which is larger than 1.21 for the case without mantle buoyancy (Figure 4a). If the surface density is reduced to 1.65×10^4 kg m^{-2}, D greatly differs from that in Figure 4a only after 4×10^7 years when the mantle buoyancy starts to dominate crustal deformation (Figure 9f).

3.5. Discussions

Our results show that for a simple crust-mantle system in which topography at the Earth's surface and Moho represents the only density anomalies, while the crust approaches an isostatic state at long wavelengths (>800 km), the state of isostasy may not be the asymptotic limit at short wavelengths that are comparable with the widths of mountain belts, depending on crustal and lithospheric rheology (Figures 5 and 8). At short-wavelengths (<300 km), when crustal viscosity is smaller than lithospheric viscosity, the crust approaches a state with significant crustal over-compensation (Figures 5a and 6a); when crustal and lithospheric viscosities are both large and comparable, the crust approaches a state with slight under-compensation (Figure 5a). Crust reaches an asymptotic state with constant D after characteristic time τ_2, and crustal

thickness variation can be maintained until τ_1 (Figures 4a and 6a). The deviation from isostasy at the asymptotic state can produce large gravity anomalies (Figure 6c) which may last for long geologic time (i.e., τ_1-τ_2 in Figures 4b and 6b). It should be pointed out that we must be cautious in interpreting the time history of topography and degree of compensation D when topography is small (Figures 4b and 6b). The models with a deformable crust presumably can only be applied when the crust has a relatively large stress. When topography becomes sufficiently small such that the resulting stress is smaller than a finite strength of crust (or faults), a deformable crust may be no longer a valid assumption [*Lambeck*, 1980].

For an effectively elastic upper crust that prevents any horizontal crustal deformation, both initial conditions and crustal and lithospheric rheology play important roles in crustal compensation at short wavelengths (Figure 7). Because the upper crust can permanently support topography, crust will eventually become undercompensated after a characteristic time τ_1 which is the decay time of Moho topography (Figures 7b and 8b). Priori to τ_1, the state of crustal compensation is mainly determined by initial conditions (i.e., degree of compensation is similar to its initial value); τ_1 is strongly dependent on viscosity and thickness of the lower crust. For a thick and weak lower crust, τ_1 can be as small as tens of million years at short wavelengths; for a moderately strong lower crust, τ_1 can be as large as one billion years (Figure 8b). The results for an elastic upper crust and a weak lower crust are consistent with the results of *Kusznir and Matthews* [1988].

In order to have the state of isostasy as an asymptotic state, the ratio of vertical velocity at the surface to vertical velocity at the Moho in the asymptotic state must be identical to $(\rho_m - \rho_c)/\rho_c$, when both the surface and Moho topography decay with time. Clearly, this ratio of vertical velocities in the asymptotic state depends on crustal and lithospheric rheological structure and wavelength. Deviation from isostasy arises when the viscosity structure and wavelength lead to a ratio of vertical velocities which differs from $(\rho_m - \rho_c)/\rho_c$. The crustal compensation with a moderately high viscosity crust can also be understood in terms of coupling between crustal buoyancy forces and mantle flow. A weak lower crust reduces the coupling between the Moho and surface; consequently, mass anomaly associated with the variations in Moho topography cannot be effectively compensated onto the surface, and part of this mass anomaly is compensated by mantle flow. Increasing either viscosity or thickness of lithosphere, or crustal thickness results in a stronger coupling between mass anomaly on the Moho and mantle flow, thus enhancing the deviation from isostasy (Figure 5a). Increasing viscosity in the lower crust enhances the coupling between the Moho and surface and reduces the deviation from isostasy (Figure 5a). The physics of the coupling is similar to that in studies on long wavelength dynamic topography and geoid [*Hager and Richards*, 1989].

Although these models may be limited for understanding crustal dynamics in regions where crustal deformation is predominantly caused by external forces which are not considered in this study (e.g., actively building mountain belts due to crustal shortening), they may have implications to the evolution of postorogeny or orogenic belts where external forces have a diminishing influence. Models with a moderately high viscosity upper crust may be proper for regions that remain tectonically active, while models with an effectively elastic upper crust may be applicable to old and tectonically stable regions. Relatively young mountain belts

with overcompensated crust (e.g., the eastern Tian Shan) may result from a crust that is weaker than the underlying mantle. Excess Moho topography beneath old orogenic belts (e.g., the Appalachian) may be a consequence of a relatively strong lower crust and lithosphere that help preserve an initially overcompensated crustal structure. The absence of roots at the Moho underneath old orogenic belts (e.g., the Caledonides) may result from a relatively weak lower crust that might have existed for a long geologic time and effectively removed Moho topography, as originally suggested by *Kusznir and Matthews* [1988]. Further elaboration is difficult without having a proper thermal model that describes temperature and viscosity evolution within crust and lithosphere.

It should be pointed out that our results are different from *Artyushkov's* [1974] analyses that predicted crustal under-compensation. The analyses by *Artyushkov* [1974] suggested that crustal isostasy would be a stable state if density contrast across the mantle-crust boundary is the same as that on the surface. However, we found that crustal isostasy is not an asymptotic state even when the surface and mantle-crust boundary have the same density contrast. The difference may be due to the differences between these two formulations. Our models incorporate the effects of the mantle and time dependence which as we have demonstrated are crucial for crustal compensation, but these effects were not considered in *Artyushkov's* [1974] analyses.

The influence of mantle buoyancy on topography at the surface and crust-mantle boundary was studied by *Bindschadler and Parmentier* [1990] with different models. Since the topographic growth caused by horizontal shear stress of mantle flow is quite slow (Figure 9a and τ_1 in Figure 5b which is about 10^8 years), regions where topography of this origin is likely to be observed are those long-lived subduction zones. If such topography is achieved in subduction zones, the crust above the subducted slabs would show a significant over-compensation (Figure 9e). However, seismically observed crustal thickness variations in the central Andes do not seem to show significant deviation from crustal isostasy [*Beck et al.*, 1996], suggesting that topography derived from horizontal shear stress of mantle flow may not be so important for the Earth. Although the presence of mantle buoyancy complicates crustal compensation, the general trends in crustal compensation derived from models without mantle buoyancy may be used to infer subcrustal dynamics including dynamic topography induced by mantle buoyancy (Figure 9).

4. Conclusions

Analytic models for time evolution of topography at the surface and crust-mantle boundary have been formulated for a layered viscoelastic medium. The models can describe the topographic relaxation at these density interfaces in both small timescale associated with vertical crustal deformation (i.e., postglacial rebound), and large timescale associated with horizontal crustal deformation. These models are used to investigate the influences of crustal and lithospheric rheology on crustal compensation. The models show that for a simple crust-mantle system in which topography at the Earth's surface and Moho represents the only density anomalies, while the crust approaches the state of isostasy at long wavelengths (> 800 km), the state of isostasy may not be the asymptotic state for the crust at short-wavelengths, depending on crustal and lithospheric rheology. Models with two different types of

upper crust are considered: (1) upper crust with moderately high viscosity, and (2) effectively elastic and rigid upper crust.

When the overall strength of crust is weaker than lithosphere, the crust tends to approach a state with a significant overcompensation at crust-mantle boundary at wavelengths comparable with width of orogenic belts (<300 km). The overcompensated crust can produce significant negative isostatic gravity anomalies over orogenic belts. The overcompensation for deformable crust is greater for weaker crust and stronger lithosphere. A thicker crust or lithosphere also enhances the overcompensation. Slight crustal undercompensation may occur when crustal and lithospheric viscosities are both large and comparable. For effectively elastic and rigid upper crust that can permanently support topography, crust will eventually become under-compensated after a characteristic time τ_1 which is the decay time of Moho topography, consistent with results of *Kusznir and Matthews* [1988]. Priori to τ_1, degree of compensation is close to its initial value; τ_1 ranges from tens of million years to one billion years and is strongly dependent on viscosity and thickness of the lower crust. These models may be useful for understanding the evolution of postorogeny or orogenic belts where external forces (e.g., crustal shortening) have a diminishing influence.

Appendix: Solution of Time-Dependent Topography at Top, Moho, and Bottom Boundaries in a Maxwellian Medium

After a Laplace transformation, (2) and (5) keep the same mathematic forms, and (4) becomes

$$\tilde{\bar{\sigma}}(s) = -\bar{P}(s)\hat{I} + \eta(s)\nabla\tilde{\bar{u}}(s), \qquad (\text{A1})$$

where $\bar{P}(s) = \bar{p}(s)/(1+s\tau)$, $\eta(s) = \eta/(1+s\tau)$, $\tau = \eta/\mu$ is the Maxwell time for this layer, the tilt stands for the Laplace transform of the corresponding function, and s is the Laplace transform variable. Equations (2), (5), and (A1) have the same mathematic form as those for purely viscous flow. We can apply the Fourier series and propagator matrix techniques to solve these equations as done for viscous flow [e.g., *Cathles*, 1975; *Hager and O'Connell*, 1981]. Since the equations are linear, we will only derive solutions for a single harmonics in the following analysis. Solutions for complex problems can be obtained by summation of different harmonics. Define

$$\vec{w}(s) = [\tilde{u}_z(s), \tilde{u}_x(s), \tilde{\sigma}_{zz}(s)/(2k), \tilde{\tau}_{xz}(s)/(2k)]^T, \quad (\text{A2})$$

$$\vec{b}(s) = [0, 0, \delta\bar{p}(s)/(2k), 0]^T, \qquad (\text{A3})$$

where $k = 2\pi/\lambda$ is the wavenumber, λ is the wavelength, the superscript T stands for the matrix transpose, and all variables may be a function of z, $\vec{w}(z_2,s)$ can be expressed as

$$\vec{w}(z_2,s) = P(z_2,z_1,s)\vec{w}(z_1,s) + \int_{z_1}^{z_2} P(z_2,\xi,s)\vec{b}(\xi,s)d\xi, \quad (\text{A4})$$

where z_1 and z_2 are two arbitrary points within the layer; $P(z_2,z_1,s)$ is a propagator matrix and is a function of s due to the dependence of $\eta(s)$.

In what follows, we will present a solution for a simple three-layer model with crust, lithosphere, and mantle (Figure 1), using the propagator matrix technique. For simplicity, the driving forces except those associated with topography at

density boundaries are assumed in the mantle. The following approach can be easily extended for models with more complicated buoyancy and viscosity structures. For the three-layer model, $\vec{w}$ on the Moho and the top surface can be expressed, respectively, as

$$\vec{w}(z_m,s) = P_2 P_1 \vec{w}(0,s) + P_2 \int_0^{z_l} P(z_l,\xi,s)\vec{b}(\xi,s)d\xi, \quad (A5)$$

$$\vec{w}(z_t,s) = P_3 P_2 P_1 \vec{w}(0,s) + P_3 P_2 \int_0^{z_l} P(z_l,\xi,s)\vec{b}(\xi,s)d\xi$$

$$+ P_3 \int_{z_l}^{z_m} P(z_m,\xi,s)\vec{b}(\xi,s)d\xi + \int_{z_m}^{z_t} P(z_t,\xi,s)\vec{b}(\xi,s)d\xi, \quad (A6)$$

where $P_1 = P(z_l,0,s)$, $P_2 = P(z_m,z_l,s)$ and $P_3 = P(z_t,z_m,s)$ are the propagator matrices for each layer.

We now seek the solution for the time evolution of surface topography $H_t(t)$, the Moho topography $H_m(t)$, and bottom topography $H_b(t)$, under given initial and boundary conditions. Suppose that the Moho topography $H_m(t) << \lambda$, then the buoyancy force associated with the Moho topography can be treated as a delta function $H_m(t)\Delta\rho\delta(z-z_m)$, where $\Delta\rho$ is the density contrast across the Moho (i.e., $\rho_m - \rho_c$, ρ_c and ρ_m are the densities of crust and mantle, respectively). In case that mantle buoyancy is included, the mantle buoyancy is assumed to be $\delta\rho\delta(z-z_s)H(t)$ with the same wavelength λ, where $\delta\rho$ is surface density and $H(t)$ is the Heaviside function.

On the top and bottom boundaries (i.e., $z = z_t + H_t(t)$ and $z = H_b(t)$ in Figure 1), both tangential and normal stresses are zero. If the amplitudes of surface and bottom topography are much smaller than the wavelength λ and the thickness of box D, the free-surface boundary conditions can be written as [e.g., *Cathles*, 1975; *Soloman et al.*, 1982]

$$\sigma_{xz}(0,t) = \sigma_{xz}(z_t,t) = 0, \quad (A7)$$

$$\sigma_{zz}(0,t) = (\rho_{co} - \rho_m)gH_b(t), \quad \sigma_{zz}(z_t,t) = -\rho_c g H_t(t), \quad (A8)$$

where ρ_{co} is the density of the outer core.

The initial condition is given in terms of topography at the top, Moho, and bottom boundaries as

$$H_t(z_t,0) = H_t^0, \quad H_m(z_m,0) = H_m^0, \quad H_b(0,0) = H_b^0, \quad (A9)$$

H_b^0 is set to zero in this study. On the density interfaces, kinematic conditions are

$$u_z(z_t,t) = \frac{dH_t(t)}{dt}, u_z(0,t) = \frac{dH_b(t)}{dt}, u_z(z_m,t) = \frac{dH_m(t)}{dt}, \quad (A10)$$

Since the general solutions (A5) and (A6) are in the spectral s domain, a Laplace transform is needed to perform on boundary conditions (A7) and (A8); $\tilde{u}_z(s)$ in $\vec{w}(z_t,s)$, $\vec{w}(z_m,s)$, and $\vec{w}(0,s)$ in (A5) and (A6) are substituted by the transformed kinematic conditions (A10) in which the initial conditions (A9) are used. Substituting the transformed kinematic and boundary conditions into (A5) and (A6) results in two matrix equations

$$W(z_m,s) = P_2 P_1 W(0,s) + P_2 P_1' T(s) + B(z_m,s), \quad (A11)$$

$$W(z_t,s) = P_3 P_2 P_1 W(0,s) + P_3 P_2 P_1' T(s) + P_3 B(z_m,s), \quad (A12)$$

where

$$W(z_m,s)$$

$$= [-H_m^0 + s\tilde{H}_m(s), \tilde{u}_x(z_m,s), \frac{\tilde{\sigma}_{zz}(z_m,s)}{2k}, \frac{\tilde{\sigma}_{xz}(z_m,s)}{2k}]^T, \quad (A13)$$

$$W(0,s) = [s\tilde{H}_b(s), \tilde{u}_x(0,s), \gamma_1 \tilde{H}_b(s), 0]^T, \quad (A14)$$

$$T(s) = [0,0,\delta\tilde{\rho}(s)g/(2k),0]^T, \quad (A15)$$

$$B(z_m,s) = [0,0,\gamma_2 \tilde{H}_m(s),0]^T, \quad (A16)$$

$$W(z_t,s) = [-H_t^0 + s\tilde{H}_t(s), \tilde{u}_x(z_t,s), \gamma_3 \tilde{H}_t(s),0]^T, \quad (A17)$$

$P_1' = P(z_s,0,s)$, $\gamma_1 = (\rho_{co} - \rho_m)/(2k)$, $\gamma_2 = \Delta\rho/(2k)$, and $\gamma_3 = -\rho_c/(2k)$.

Defining $A = P_2 P_1$, $B = P_3 P_2 P_1$, $C = P_3$, $D = P_2 P_1'$, $E = P_3 P_2 P_1'$, and combining the first equation in (A11) and the first three equations in (A12), we obtain a system of equations

$$\begin{bmatrix} A_{11}s + A_{13}\gamma_1 & A_{12} & -s & 0 \\ B_{11}s + B_{13}\gamma_1 & B_{12} & \gamma_2 C_{13} & -s \\ B_{31}s + B_{33}\gamma_1 & B_{32} & \gamma_2 C_{33} & -\gamma_3 \\ B_{41}s + B_{43}\gamma_1 & B_{42} & \gamma_2 C_{43} & 0 \end{bmatrix} \begin{bmatrix} \tilde{H}_b(s) \\ \tilde{u}_x(0,s) \\ \tilde{H}_m(s) \\ \tilde{H}_t(s) \end{bmatrix}$$

$$= \begin{bmatrix} -H_m^0 - D_{13}\delta\tilde{\rho}(s)g/(2k) \\ -H_t^0 - E_{13}\delta\tilde{\rho}(s)g/(2k) \\ -E_{33}\delta\tilde{\rho}(s)g/(2k) \\ -E_{43}\delta\tilde{\rho}(s)g/(2k) \end{bmatrix}. \quad (A18)$$

From (A18), we can determine $\tilde{H}_b(s)$, $\tilde{u}_x(0,s)$, $\tilde{H}_m(s)$, and $\tilde{H}_t(s)$. We can then solve the reverse Laplace transform to obtain the solution in time domain by applying a residue theory. As an example, we show the solution procedure for $H_t(t)$ as follow. From (A18), $\tilde{H}_t(s)$ can be expressed as

$$\tilde{H}_t(s) = \frac{\det[K_t(s)]}{\det[K(s)]} = \frac{Q(s)}{N(s)}, \quad (A19)$$

where det stands for determinant, $K(s)$ is the 4x4 matrix in (A18), and $K_t(s)$ is the same matrix but with the last column being replaced by the right-hand-side vector in (A18). $\det[K(s)] = 0$ is the equation for eigenvalues, and for the model with three density interfaces and two viscosity interfaces there are seven eigenvalues [*Han and Wahr*, 1995; *Fang and Hager*, 1995]. If there are no repeated eigenvalues, the residue theory can be readily applied to give the solution in time domain,

$$H_t(t) = \sum_{i=1}^{7} \frac{Q(s_i)}{N'(s_i)} \exp(s_i t), \quad (A20)$$

where $N'(s_i) = dN/ds|_{s=s_i}$. Each eigenvalue s_i represents a deformation mode whose characteristic decay time is determined by s_i. It should be pointed out that the eigenvalues are only dependent on the viscosity and density structures of the model. After the time dependence of topography is obtained, time dependence of velocity and stress can be determined from (A4)-(A6).

References

Artyushkov, E. V., Can the Earth's crust be in a state of isostasy, *J. Geophys. Res.*, *79*, 741-752, 1974.

Avouac, J. P., and E. V. Burov, Erosion as a driving mechanism of intracontinental mountain growth, *J. Geophys. Res.*, *101*, 17747-17769, 1996.

Banks, R. J., R. L. Parker, and J. P. Huestus, Isostatic compensation on a continental scale: Local versus regional mechanisms, *Geophys. J. R. Astron. Soc.*, *51*, 431-452, 1977.

Barrell, J., The strength of the Earth's crust, *J. Geol.*, *22*, 425-433, 1914.

Bechtel, T. D., D. W. Forsyth, V. L. Sharpton, and R. A. F. Grieve, Variations in effective elastic thickness of the north-American lithosphere, *Nature*, *343*, 636-638, 1991.

Beck, S. L., G. Zandt, S. C. Myers, T. C. Wallace, P. G. Silver, and L. Drake, Crustal thickness variations in the central Andes, *Geology*, *24*, 407-410, 1996.

Bindschadler, D. L., and E. M. Parmentier, Mantle flow tectonics: The influence of a ductile lower crust and implications for the formation of topographic uplands on Venus, *J. Geophys. Res.*, *95*, 21329-21344, 1990.

Bird, P., Lateral extrusion of lower crust from under high topography in the isostatic limit, *J. Geophys. Res.*, *96*, 10275-10286, 1991.

Brace, W. F., and D. L. Kohlstedt, Limits on lithospheric stress imposed by laboratory experiments, *J. Geophys. Res.*, *85*, 6248-6252, 1980.

Burov, E. V., M. G. Kogan, H. Lyon-Caen and P. Monlar, Gravity anomalies, the deep structure, and dynamic processes beneath the Tien Shan, *Earth Planet. Sci. Lett.*, *96*, 367-383, 1990.

Byerlee, J. D., Friction of rocks, *Pure Appl. Geophys.*, *116*, 615-626, 1978.

Carter, N. L., and M. C. Tsenn, Flow properties of continental lithosphere, *Tectonophysics*, *136*, 27-63, 1987.

Cathles, L. M., *The Viscosity of the Earth's Mantle*, 386pp., Princeton Univ. Press, Princeton, N. J., 1975.

Chase C. G., and M. McNutt, The geoid: Effect of compensated topography and uncompensated oceanic trenches, *Geophys. Res. Lett.*, *9*, 29-32, 1982.

Dahlen, F. A., Isostatic geoid anomalies on a sphere, *J. Geophys. Res.*, *87*, 3943-3947, 1982

Daly, R. A., *Strength and Structure of the Earth*, 434pp., Prentice-Hall, Englewood Cliffs, N. J., 1940.

DeBremaecker, J. C., Is the oceanic lithosphere elastic or viscous? *J. Geophys. Res.*, *82*, 2001-2004, 1977.

Dorman, L. M., and B. T. R. Lewis, Experimental isostasy, 1, Theory of determination of the earth's isostatic response to a concentrated load, *J. Geophys. Res.*, *75*, 3357-3365, 1970.

Eddington, P. K., R. B. Smith, and C. Renggli, in *Continental Extensional Tectonics*, edited by M. P. Coward, and P. L. Hancock, Geol. Soc. Spec. Publ., 28, 371-392, 1987.

England, P., and D. McKenzie, A thin viscous sheet model for continental deformation, *Geophys. J. R. Astron. Soc.*, *70*, 295-321, 1982.

Fang, M., and B. H. Hager, The singularity mystery associated with a radially continuous Maxwell viscoelastic structure, *Geophys. J. Int.*, *123*, 849-865, 1995.

Fleitout, L., and C. Froidevaux, Tectonics and topography for a lithosphere containing density heterogeneities, *Tectonics*, *1*, 21-56, 1982.

Grimm, R. E., and S. C. Soloman, Viscous relaxation of impact crater relief on Venus: Constraints on crustal thickness and thermal gradient, *J. Geophys. Res.*, *93*, 11911-11929, 1988.

Gunn, R., A quantitative evaluation of the influence of the lithosphere on the anomalies of gravity, *J. Franklin Inst.*, *236*, 373-396, 1943.

Gurnis, M., Depressed continental hypsometry behind oceanic trenches: A clue to subduction controls on sea-level change, *Geology*, *21*, 29-32, 1993.

Hager, B. H., and R. O'Connell, A simple global model of plate dynamics and mantle convection, *J. Geophys. Res.*, *86*, 4843-4867, 1981.

Hager, B. H., and M. A. Richards, Long-wavelength variations in Earth's geoid: physical models and dynamical implications, *Phil. Trans. R. Soc. Lond.*, *328*, 309-327, 1989.

Han, D. and J. Wahr, The viscoelastic relaxation of a realistically stratified earth and a further analysis of post-glacial rebound, *Geophys. J. Int.*, *120*, 287-311, 1995.

Haskell, N. A., The motion of a viscous fluid under a surface load 2, *Physics*, *7*, 56-61, 1936.

Heiskanen, W. A., and F. A. Vening-Meinesz, *The Earth and Its Gravity Field*, McGraw-Hill, New York, 1958.

Jeffreys, H., *The Earth*, Cambridge Univ. Press, New York, 1970.

Jones, C. H., J. R. Unruh, and L. J. Sonder, The role of gravitational potential energy in active deformation in the southwestern United States, *Nature*, *381*, 37-41, 1996.

Jin, Y., M. McNutt, and Y. S. Zhu, Evidence from gravity and topography data for folding of Tibet, *Nature*, *371*, 669-674, 1994.

Kanamori, H., The state of stress in the Earth's lithosphere, *Phys. Earth's Inter.*, 531-554, 1980.

Karato, S., and P. Wu, Rheology of the upper mantle: A synthesis, *Science*, *260*, 771-778, 1993.

Kusznir, N. J., and D. H. Matthews, Deep seismic reflections and the deformational mechanics of the continental lithosphere, *J. Petrol.*, Special Lithosphere Issue, 64-87, 1988.

Lambeck, K., Estimates of stress differences in the crust from isostastic considerations, *J. Geophys. Res.*, *85*, 6397-6402, 1980.

Lenardic, A., and W. M. Kaula, More thoughts on convergent crustal plateau formation and mantle dynamics with regard to Tibet, *J. Geophys. Res.*, *100*, 15193-15203, 1995.

Liu, H. P., and D. Kosloff, Elastic-plastic bending of the lithosphere incorporating rock deformation data, with application to the structure of the Hawaiian archipelago, *Tectonophysics*, *50*, 249-274, 1978.

McNutt, M., Implications of regional gravity for state of stress in the Earth's crust and upper mantle, *J. Geophys. Res.*, *85*, 6377-6396, 1980.

Melosh, H. J., and A. Raefsky, The dynamical origin of subduction zone topography, *Geophys. J. R. Astron. Soc.*, *60*, 333-354, 1980.

Morgan, W. J., Gravity anomalies and convection currents, 1, A sphere and cylinder sinking beneath the surface of a viscous fluid, *J. Geophys. Res.*, *70*, 6175-6187, 1965.

Parsons, B., and J. G. Sclater, An analysis of the variation of ocean floor bathymetry and heat flow with age, *J. Geophys. Res.*, *82*, 803-827, 1977.

Peltier, W. R., The impulse response of a Maxwell Earth, *Rev. Geophys.*, *12*, 649-669, 1974.

Soloman, S. C., R. P. Comer, and J. W. Head, The evolution of impact basins: viscous relaxation of topographic relief, *J. Geophys. Res.*, *87*, 3975-3992, 1982.

Turcotte, D. L., and G. Schubert, *Geodynamics*, pp.121-123, John Wiley, New York, 1982.

Walcott, R. I., Flexural rigidity, thickness, and viscosity of the lithosphere, *J. Geophys. Res.*, *75*, 3941-3954, 1970.

Watts, A. B., and M. Talwani, Gravity anomalies seaward of deep-sea trenches and their tectonic implications, *Geophys. J. R. Astron. Soc.*, *36*, 57-90, 1974.

Watts, A. B., J. H. Bodine, and N. M. Ribe, Observations of flexure and the geological evolution of the Pacific Ocean basin, *Nature*, *283*, 532-537, 1980.

Wdowinski, S., and R. J. O'Connell, Deformation of the central Andes derived from a flow model of subduction zones, *J. Geophys. Res.*, *96*, 12245-12255, 1991.

Wernicke, B., *et al.*, Origin of high mountains in the continents: the southern Sierra Nevada, *Science*, *271*, 190-193, 1996.

Wu, P., Viscous versus viscoelastic deformation and the advection of pre-stress, *Geophys. J. Int.*, *108*, 136-142, 1992.

Wu, P., and W. R. Peltier, Viscous gravitational relaxation, *Geophys. J. R. Astron. Soc.*, *70*, 435-485, 1982.

Zuber, M. T., T. D. Bechtel, and D. W. Forsyth, Effective elastic thickness of the lithosphere and mechanisms of isostastic compensation in Australia, *J. Geophys. Res.*, *94*, 9353-9367, 1989.

S. Zhong, Seismological Laboratory, 252-21, California Institute of Technology, Pasadena, CA 91125. (e-mail: zhong@gps.caltech.edu)